RESEARCH ARTICLE
ATMOSPHERIC PHYSICS

Earth and Planetary Physics
8: 497–513, 2024
doi: 10.26464/epp2024027

Influence of topography on the fine structures of stratospheric gravity waves: An analysis using COSMIC-2 temperature data

JiaRui Wei[1,2], Xiao Liu[1,3*], JiYao Xu[1,2*], QinZeng Li[1,2], and Hong Gao[1,2]

[1]State Key Laboratory of Space Weather, National Space Science Center, Chinese Academy of Sciences, Beijing 100190, China;

[2]University of Chinese Academy of Sciences, Beijing 100049, China;

[3]Institute of Electromagnetic Wave, School of Physics, Henan Normal University, Xinxiang Henan 453000, China

Key Points:

- Fine structures of the geographic distribution of gravity waves are revealed from dense COSMIC-2 samplings in the upper troposphere and stratosphere.
- Dissipation layers, which are above the tropopause jet, provide the body force to generate secondary gravity waves, especially above topographic regions.
- The Tibetan Plateau and Andes have high elevations, with strong peaks of gravity wave potential energy above them, whereas the Rocky, Atlas, Caucasus, and Tianshan Mountains have weak peaks above them.

Citation: Wei, J. R., Liu, X., Xu, J. Y., Li, Q. Z., and Gao, H. (2024). Influence of topography on the fine structures of stratospheric gravity waves: An analysis using COSMIC-2 temperature data. *Earth Planet. Phys.*, *8*(3), 497–513. http://doi.org/10.26464/epp2024027

Abstract: We derive the potential energy of gravity waves (GWs) in the upper troposphere and stratosphere at 45°S–45°N from December 2019 to November 2022 by using temperature profiles retrieved from the Constellation Observing System for Meteorology, Ionosphere, and Climate-2 (COSMIC-2) satellite. Owing to the dense sampling of COSMIC-2, in addition to the strong peaks of gravity wave potential energy (GWPE) above the Andes and Tibetan Plateau, we found weak peaks above the Rocky, Atlas, Caucasus, and Tianshan Mountains. The land–sea contrast is responsible for the longitudinal variations of the GWPE in the lower and upper stratosphere. At 40°N/S, the peaks were mainly above the topographic regions during the winter. At 20°N/S, the peaks were a slight distance away from the topographic regions and might be the combined effect of nontopographic GWs and mountain waves. Near the Equator, the peaks were mainly above the regions with the lowest sea level altitude and may have resulted from convection. Our results indicate that even above the local regions with lower sea level altitudes compared with the Andes and Tibetan Plateau, the GWPE also exhibits fine structures in geographic distributions. We found that dissipation layers above the tropopause jet provide the body force to generate secondary waves in the upper stratosphere, especially during the winter months of each hemisphere and at latitudes of greater than 20°N/S.

Keywords: topography; fine structures; stratospheric gravity waves; Constellation Observing System for Meteorology; Ionosphere and Climate-2 (COSMIC-2); dissipation layers

1. Introduction

Atmospheric gravity waves (GWs) radiate from the periodic oscillations of air parcels caused by the unbalanced forces of gravity and buoyancy. The sources of these oscillations may be flow over topography, convection, strong wind jets and shear, body forcing generated by localized wave dissipation, wave–wave interactions, and nonlinear external forces (Fritts and Alexander, 2003). As a result of the conservation of momentum and energy, the amplitude of atmospheric GWs increases exponentially with increasing height before dissipation, instability, and breakdown (Hines, 1960). Unstable or breaking GWs deposit their momentum and energy into the background atmosphere, thereby changing the atmospheric structure and circulation as well as the chemical processes and electrodynamics in the neutral atmosphere and ionosphere (Holton, 1983; Shepherd, 2002; Fritts and Alexander, 2003; Hecht, 2004). Recent studies have shown that broken GWs can transition into small-scale waves and turbulence (Fritts et al., 1994; Isler et al., 1994; Fritts and Alexander, 2003). Subsequently, the momentum deposited by small-scale waves and turbulence provides a body force for generating large-scale secondary GWs (Vadas and Fritts, 2002; Heale et al., 2020). These large-scale secondary GWs have longer wavelengths and faster phase speeds, and thus can propagate into wider vertical and horizontal ranges (Trinh et al., 2018; Vadas et al., 2018). This in turn influences the neutral atmosphere and the ionosphere over a wide spatial region

First author: J. R. Wei, 15286878920@139.com
Correspondence to: X. Liu, liuxiao@htu.edu.cn
J. Y. Xu, xujy@nssc.ac.cn
Received 18 JAN 2024; Accepted 02 APR 2024.
First Published online 29 APR 2024.

(Trinh et al., 2018). Therefore, it is important to characterize GWs and secondary GWs in observations and models.

Ground-based observations, such as from a sounding rocket (Eckermann et al., 1995), radiosonde (Wang L and Geller, 2003), radar (Tsuda et al., 1990; Sato, 1993), lidar (Hertzog et al., 2001), and aircraft (Fritts and Nastrom, 1992), have provided valuable wind and temperature data for studying atmospheric GWs at different atmospheric layers and locations with (nearly) continuous local-time coverage. However, because of the limited geographical distribution of ground-based observations, it is difficult to obtain the global distribution of atmospheric GWs. On the other hand, satellite observations provide nearly global coverage and can be used to study global atmospheric GWs. The wavelength spectra of atmospheric GWs observed by satellites are dependent on the viewing mode (as shown in Fig. 9 of Preusse et al., 2008). The nadir viewing mode (e.g., the Atmospheric Infrared Sounder [AIRS] on the National Aeronautics and Space Administration's [NASA's] Aqua satellite) has the advantage of a high horizontal resolution and can resolve atmospheric GWs with long vertical wavelengths (Hoffmann et al., 2013; Ern et al., 2017). The limb-viewing mode (e.g., the radio occultation [RO] profiles retrieved from the Global Navigation Satellite System [GNSS]) has the advantage of high vertical resolution and can resolve atmospheric GWs with long horizontal wavelengths (Kursinski et al., 1997; Rocken et al., 1997; Alexander et al., 2008a, b).

Historically, the RO technique has been used to sound planetary atmospheres and ionospheres (Fjeldbo et al., 1971). Radio occultation profiles have the advantage of high vertical resolution in the troposphere and stratosphere. For example, the Global Positioning System/Meteorology (GPS/MET) experiment (Preusse et al., 2000; Tsuda et al., 2000) provides 100–150 RO profiles per day. These profiles have a vertical resolution of 1 km and 200–500 m in the stratosphere and troposphere, respectively, and have a 100-km horizontal resolution with an average temperature error of 0.5 ± 1.5 K at 5–40 km (Kursinski et al., 1997; Rocken et al., 1997). The Challenging Minisatellite Payload (CHAMP) mission (Ratnam et al., 2004; Hei et al., 2008) provided approximately 230 occultations per day at 0–50 km (Wickert et al., 2001; Ratnam et al., 2004). The vertical resolution of the temperature profiles ranges from 0.5 km in the lower troposphere to ~1.5 km in the stratosphere, and the horizontal resolution along the RO path is approximately a few hundred kilometers. The retrieved temperature bias is <0.5 K between 10 and 30 km (Wickert et al., 2001). The Gravity Recovery and Climate Experiment (GRACE) mission (Wickert et al., 2005) provided approximately 200–250 occultations per day. The Constellation Observing System for Meteorology, Ionosphere, and Climate (COSMIC) mission provided 2000–2500 RO events every day. The daily RO events have been reduced to more than 1000 at 5–40 km since 2011 (Anthes et al., 2008). The vertical resolution of the temperature profiles is <1 km in the troposphere (0.5 km and 1.5 km in the lower and upper troposphere, respectively; Hori-nouchi and Tsuda, 2009). The observed temperature error is 0.15 K and 0.4 K at 10–20 km and 35 km, respectively (Scherllin-Pirscher et al., 2011).

Previous studies on atmospheric GWs in the upper troposphere and stratosphere have shown high correlations between the topography and the strength of atmospheric GWs, as indicated by the gravity wave potential energy (GWPE) during preferred seasons. For example, strong GW activity occurred over the Andes during the austral winter (Ern et al., 2004; Hei et al., 2008; Yan XP et al., 2010; Faber et al., 2013; Hindley et al., 2015; Zeng XY et al., 2017) and over the Tibetan Plateau (Alexander et al., 2008a; Hei et al., 2008; Yan XP et al., 2010; Zeng XY et al., 2017) and Rocky Mountains during the boreal winter (Alexander et al., 2008a; Yan XP et al., 2010). The seasonal dependencies of the high correlations between the GWPE and topography indicate that the background atmospheric structure, especially the height variations of winds, significantly influences the vertical propagation of topography-generated atmospheric GWs. Moreover, atmospheric GWs were stronger in tropical regions in all seasons. Specifically, the peaks of atmospheric GWs shifted from ~10°N during the boreal summer to ~10°S during the austral summer (Tsuda et al., 2000; Ratnam et al., 2004; Hoffmann et al., 2013; John and Kumar, 2013).

The GWPE is the gravity wave potential energy per unit mass. The height variations of the GWPE should be proportional to $e^{z/2H_A}$ based on wave-energy conservation if there is no dissipation (Bretherton, 1966; Marks and Eckermann, 1995). Here, z and H_A denote the height and the scale height of the background atmosphere, respectively. Observational studies have shown that the GWPE increases with height but with a scale height (H_{GW}) higher than H_A (Alexander et al., 2011; Liu X et al., 2014, 2022), indicating the dissipation of atmospheric GWs in regions with a higher H_{GW}. Above the dissipation layer, atmospheric GWs can be observed again, but their characteristics are different from those below the dissipation layer. Kogure et al. (2020) directly observed secondary GWs generated by breaking mountain waves (MWs) from July 24 to 25, 2017. This event was observed by the AIRS in the stratosphere and the Visible Infrared Imaging Radiometer (VIIRS) in the mesosphere. From 18:32 to 18:42 universal time (UT) on July 24, 2017, the AIRS captured an MW event with a significant brightness temperature amplitude (3 K) and a horizontal wavelength (~500 km) over the southern Andes. During this event, no perturbations were captured by the VIIRS. However, a concentric ring GW with a wavelength of ~100 km was observed by the VIIRS in the lee of the southern Andes at 04:30 UT on July 25, 2017. The ray-tracing results indicated that the concentric ring GW may have been a secondary GW generated by the breaking of the MW in the stratosphere. Liu X et al. (2019) showed the seasonal and height dependencies of primary MWs and higher scale secondary GWs over the Andes by using temperature profiles measured by the Sounding of the Atmosphere using Broadband Emission Radiometry (SABER) instrument onboard the Thermosphere Ionosphere Mesosphere Energetics and Dynamics (TIMED) satellite from 2002 to 2017. They showed that GWs had a strong peak over the Andes and extended from 30 to ~55 km in the austral winter. This peak weakened in the height range of 55–65 km and then became stronger and tilted westward above ~65 km because of the secondary GWs generated by the broken MWs.

Because of the limited availability of sampling profiles per day and the global complex topography distribution, detailed correlations between topographies and strengths of atmospheric GWs have not been resolved until now. Previously unknown were the geographic variations and seasonal dependencies of atmospheric GWs over the Tibetan Plateau and Atlas, Caucasus, and Tianshan Mountains, which cover a wide range of latitude and longitude,

and the atmospheric GWs over the Rocky Mountains. The effects of these complex topographies on GWs had not been adequately studied. In addition, the global distribution and seasonal dependencies of the dissipation of GWs and secondary GWs in the lower stratosphere have not been adequately examined. The dense sampling profiles of the Constellation Observing System for Meteorology, Ionosphere and Climate-2 (COSMIC-2) provide a good opportunity to study the geographic variations and seasonal dependencies of MWs above the Tibetan Plateau and Rocky, Atlas, Caucasus, and Tianshan Mountains. Height variations in the GWPE can reveal the dissipation and secondary generation of atmospheric GWs in the stratosphere.

The remainder of this article is organized as follows. Data and methods for extracting GWs are introduced in Section 2. Section 3 presents maps of the GWs and their variations in longitude and height. The discussion and conclusions are presented in Sections 4 and 5, respectively.

2. Data and Methods

2.1 Data

The recent COSMIC-2 mission was composed of six satellites with next-generation GNSS RO payloads launched into a low Earth orbit on June 25, 2019. The COSMIC-2 mission has provided approximately 4000 temperature profiles since September 2019 (Anthes and Schreiner, 2019; Schreiner et al., 2020), and this number has increased to approximately 6000 since May 2021 (Randel et al., 2021). These profiles have a vertical resolution of 0.05 km below or 0.1 km above a 10 km height and error of less than 0.05 K (Schreiner et al., 2020). Compared with previous missions, the COSMIC-2 mission provides many more temperature profiles at 40°S–40°N per day.

Figure 1a shows a map of the sampling locations of the COSMIC-2 temperature profiles on October 1, 2019. The RO profiles are mostly in the latitude range of 40°S–40°N (~70% of the profiles can be judged from Figure 1b) and 20°S–20°N (see also Figure 2 of

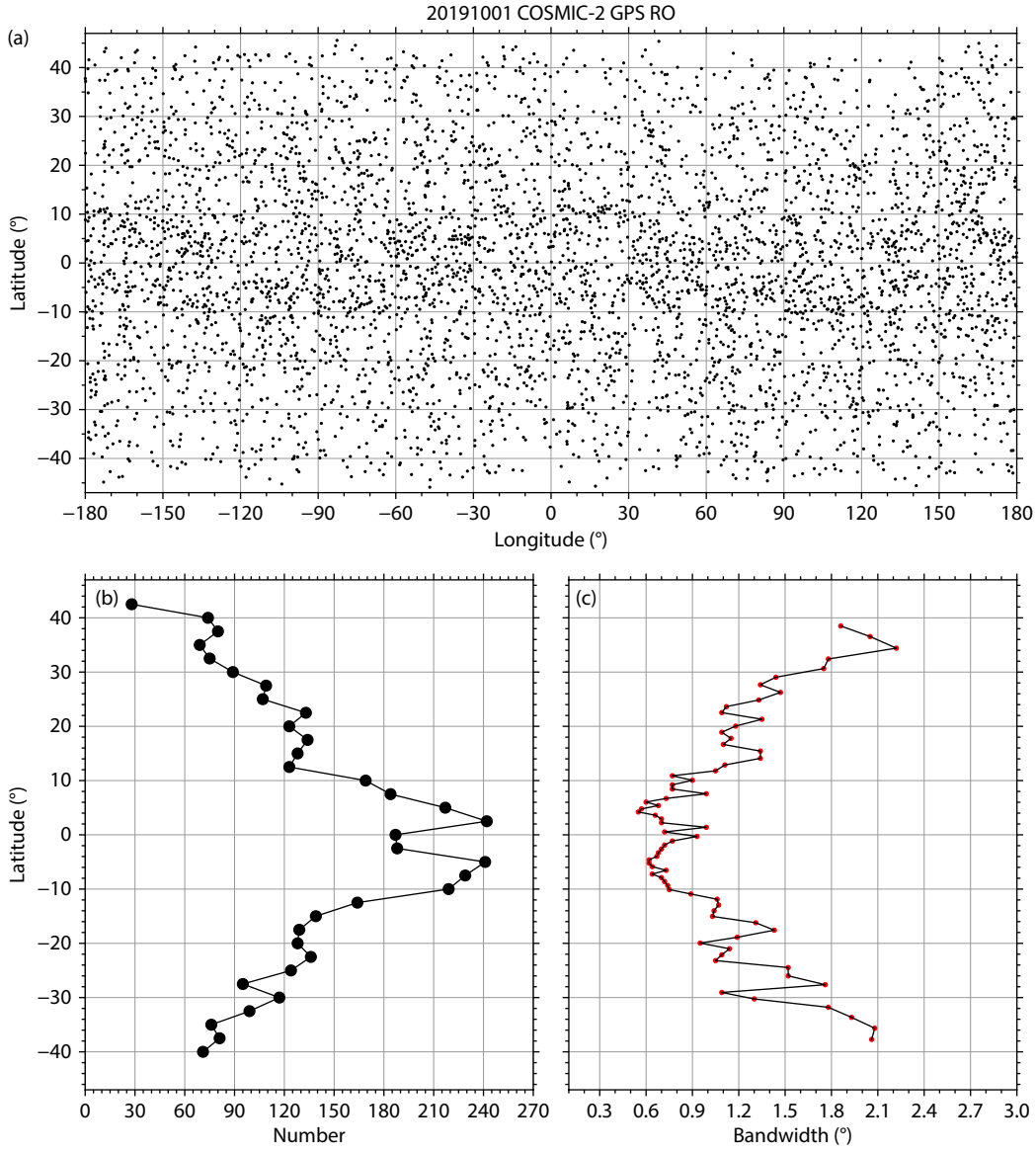

Figure 1. Sampling locations of COSMIC-2 temperature profiles (a) and their latitudinal dependence (b, c) on October 1, 2019. (b) Profile numbers in each latitudinal band with a fixed width of 2.5°. (c) Width of each latitudinal band with 60 profiles.

Ho et al., 2020). We analyzed the COSMIC-2 temperature profiles (the so-called wet temperatures) over altitudes of ~0–60 km. Data were obtained from the COSMIC Data Analysis and Archive Center (CDACC) website (https://cdaac-www.cosmic.ucar.edu/). Before further analysis was performed, each temperature profile was interpolated within a height range of ~8–60 km at intervals of 0.1 km. The upper limit of 60 km was used only in the procedure for extracting GW profiles. The physical analysis was limited to 8–50 km because of the lower signal-to-noise ratio of the RO profiles above 50 km (Hindley et al., 2015) and the edge effect of the method.

To explore the physics of GWs, we used wind data from the Modern-Era Retrospective Analysis for Research and Application, Version 2 (MERRA-2), a new version of the atmospheric reanalysis dataset developed by NASA's Global Modeling and Assimilation Office (Gelaro et al., 2017). The MERRA-2 exhibits good consistency with the monthly mean zonal wind in Singapore (Coy et al., 2016) and subtropical and polar jets obtained by using other reanalysis data (e.g., MERRA, European Centre for Medium-Range Weather Forecasts Re-Analysis Interim [ERA-Interim], Japanese 55-year Reanalysis [JRA-55], and National Centers for Environmental Prediction Climate Forecast System Reanalysis [NCEP CFSR] data; Manney and Hegglin, 2018). The MERRA-2 data were obtained from https://goldsmr5.gesdisc.eosdis.nasa.gov/data/MERRA2/M2I3NVASM.5.12.4/.

2.2 Extraction of GW

The GW extraction method used in this study was similar to those proposed by Fetzer and Gille (1994), Preusse et al. (2009), Ern et al. (2011), and Liu X et al. (2017, 2019, 2020). The detailed procedure for deriving the GW from COSMIC-2 temperature profiles is described in the following four steps. The COSMIC-2 temperature data from October 1, 2019, are used as an example to illustrate the method:

(1) Dividing latitudinal bands. If we fix the bandwidth, the sampling profiles will be different in different latitudinal bands because of the nonuniform latitudinal sampling of COSMIC-2. For example, Figure 1b shows that at a bandwidth of 2.5° the number of profiles is ~240 near the Equator, but it is only ~30 at 40°N/S. This induces a smoother fitting background and higher residuals near the Equator than at higher latitudes. Consequently, larger residuals will induce unrealistically higher GW amplitudes. To

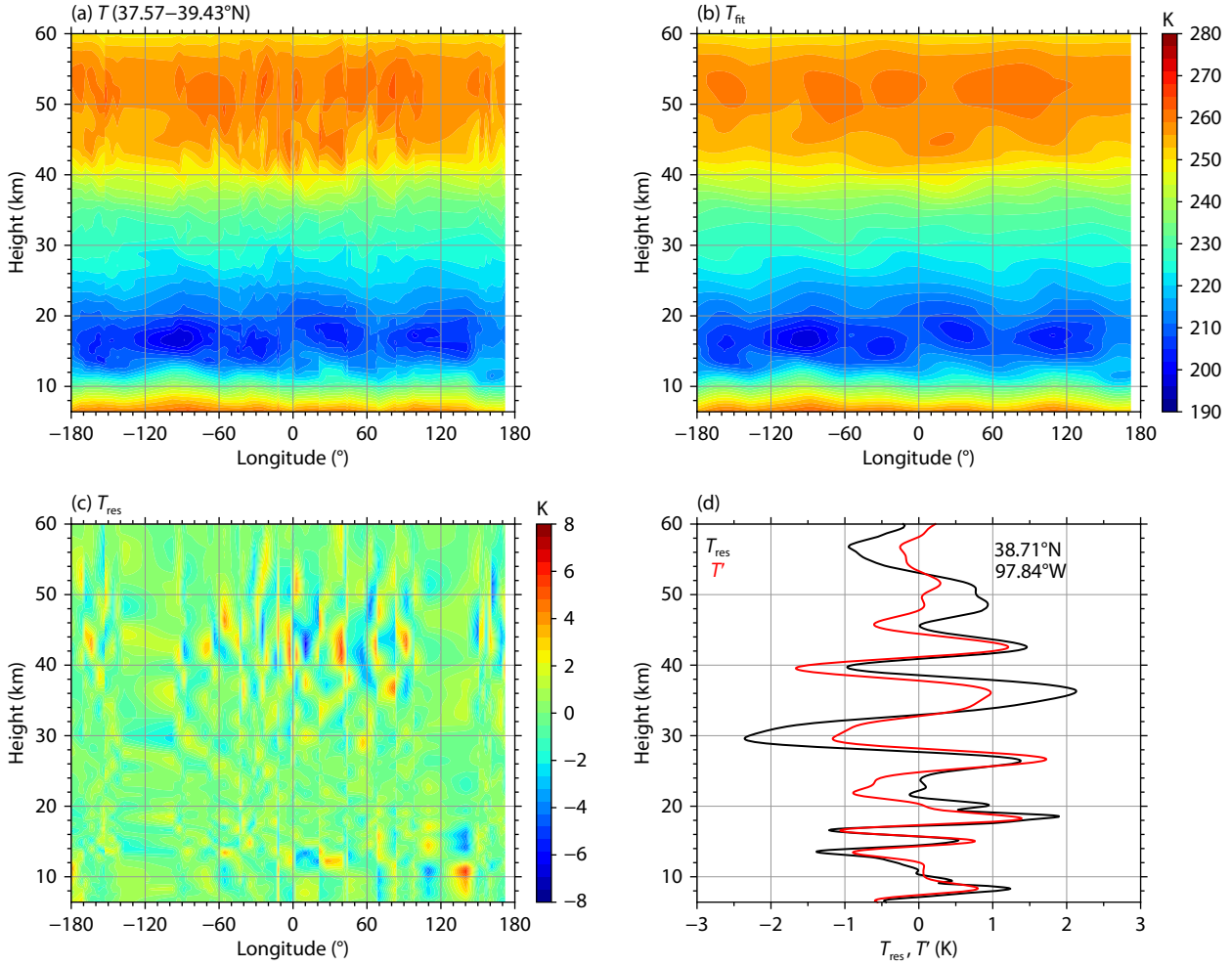

Figure 2. Procedure for the extraction of profiles of GWs from COSMIC-2 temperature profiles in the latitudinal band of 37.57–39.43°N on October 1, 2019. (a) Longitude–height distributions of the observed temperature (T). (b) Fitted temperature (T_{fit}). (c) Temperature residual ($T_{res} = T - T_{fit}$). (d) Temperature residual profile (T_{res}, black line) and GW profile (T', red line) at (38.71°N, 97.84°W).

obtain consistent fitting results for all latitudes, we used a flexible bandwidth containing ~60 profiles. The flexible bandwidth is ~0.5° near the Equator and is ~2.0° at 40°N/S (Figure 1c). Each latitudinal band contained ~60 profiles to preserve the accuracy of the least squares harmonic fitting (Lomb, 1976) in the next step.

(2) Decomposing the background temperature, large-scale fluctuations (tidal and planetary waves), and small-scale fluctuations. At each latitudinal band and height, the sampled temperature (Figure 2a) was fitted using harmonics with the background temperature $\bar{T}$ (zonal wave number 0) and large-scale fluctuations (zonal wave numbers 1–6). The fitted results ($T_{\rm fit}$) include zonal wave numbers of 0–6 (shown in Figure 2b), and the temperature residual profiles ($T_{\rm res}$, Figure 2c and the black line in Figure 2d) are regarded as small-scale fluctuations.

(3) Reconstructing GW profiles from $T_{\rm res}$ within vertical wavelengths of 2–10 km. Because the GW amplitude and wavelengths are height dependent, a continuous wavelet transform (Torrence and Compo, 1998) was performed on each $T_{\rm res}$ profile. The GW profile (T', red line in Figure 2d) was then obtained by using the inverse continuous wavelet transform and restricting the vertical wavelengths in the range of 2–10 km.

(4) Calculating the GWPE per unit mass (E_p) of each GW profile by using the following formulae (Tsuda et al., 2000; Wang L and Geller, 2003; Liu X et al., 2014, 2017):

$$E_p = \frac{1}{2}\left(\frac{g}{N}\right)^2\left(\frac{\hat{T}}{\bar{T}}\right)^2, \tag{1}$$

where $g = 9.80665\ \mathrm{m/s^2}$ is the gravitational acceleration. The Brunt–Väisälä frequency N in Equation (1) is calculated by using

$$N = \left[\frac{g}{\bar{T}}\left(\frac{\partial\bar{T}}{\partial z} + \frac{g}{c_p}\right)\right]^{1/2}. \tag{2}$$

The unit of N is $\mathrm{s^{-1}}$, $c_p = 1004.5$ J/kg/K is the specific heat of dry air at a constant pressure, and z is the altitude. The GW amplitude ($\hat{T}$) can be obtained through the Hilbert transform on the GW profile T' (Schoon and Zülicke, 2018).

To illustrate the global distribution of GWPE and its latitudinal and seasonal dependencies, the global GWPE was averaged for each bin and month of a composite year. Each bin had a size of 5° × 5° (latitude × longitude) and an overlap of 2.5° for both latitude and longitude. We focused on the GWPE from 45°S to 45°N. The month of a composite year was defined as the number of months from 2020 to 2022. For example, the GWPE in January of a composite year is the GWPE averaged for January 2020, 2021, and 2022.

3. Global Distribution of GWPE

To illustrate the global distribution of GWPE and its latitudinal and seasonal dependencies, the four seasons are the boreal spring (March–May), boreal summer (June–August), boreal autumn (September–November), and boreal winter (December–February). And the five latitudinal bands are 40°S (30–45°S), 20°S (10–30°S), 0°N/S (Equator, 10°S–10°N), 20°N (10–30°N), and 40°N (30–45°N), respectively. According to the characteristics of the GWPE, we classified the stratosphere into three layers: lower stratosphere (below ~20 km), middle stratosphere (~20–30 km), and upper stratosphere (~30–50 km).

3.1 Seasonal Dependencies of Global GWPE

Comparisons of the GWPE among three height ranges (10–20 km, 20–30 km, 30–40 km) showed that the magnitudes of GWPE at 10–20 km (not shown in here) were generally larger than those at 20–30 km and at 30–40 km (not shown in here). The GWPE at 10–20 km was strongest at latitudes higher than 25°N/S and stronger around the Equator in almost all months and longitudes. In contrast, GWPEs at 20–30 km and at 30–40 km exhibited similar monthly and longitudinal dependencies. Therefore, the GWPE in the 20–30 km stratosphere height range was more representative of the distributions of GWs in the stratosphere. Thus, we show in Figure 3 the maps of the monthly average GWPE in the 20–30 km range in a composite year.

The magenta contour lines show the monthly mean zonal wind in the same period and height range of the GWPE. The main features of the GWPE can be described over three latitudinal bands (latitudes higher than 25°N and 25°S, and 25°S–25°N).

First, at latitudes higher than 25°N, the GWPE over the Tibetan Plateau (70°E–120°E) was larger (~5–10 J/kg) or smaller (<3 J/kg) in the boreal winter or summer when the zonal winds were eastward, with peaks of higher or lower than 10 m/s. This finding is consistent with the results of previous studies (Alexander et al., 2008a; Hei et al., 2008; Faber et al., 2013; Zeng XY et al., 2017). Unlike previous studies, over the Rocky Mountains (100°–120°W), the GWPE had a weak peak (~3–5 J/kg) from November to March when the zonal winds were ~10–20 m/s. Previous studies showed that the GWPE above the Rocky Mountains had no higher peak in the boreal winter at 17–23 km (with magnitudes of ~1.2–1.6 J/kg; Alexander et al., 2008a), at 22–32 km (with magnitudes of ~1.4–1.7 J/kg; Yan XP et al., 2010), or at 12–19 km (Hei et al., 2008).

Second, at latitudes higher than 25°S, the GWPE in the region of the Andes (40°W–80°W) was strong (~10–15 J/kg) in the austral winter when the zonal winds were eastward and faster than 10 m/s. In contrast, the GWPE over the Andes was weak in the austral summer when the zonal winds were eastward but slower than 10 m/s. This finding is consistent with the results of previous studies (Hei et al., 2008; Yan XP et al., 2010; Faber et al., 2013; Hindley et al., 2015; Ern et al., 2018).

Finally, over the tropical regions (25°S–25°N), the GWPE was stronger (~3–10 J/kg) throughout the composite year than at latitudes higher than 25°N and 25°S. The GWPE was relatively small (~3–5 J/kg) when the zonal winds were almost zero in the boreal autumn. Moreover, the longitudinal variations in these strong GWPE depended on the season. In the boreal spring and autumn, the GWPE peaks were strong near the Equator (10°S–10°N). In the boreal summer or winter, the peaks of GWPE were stronger or weaker at 0°–20°N than at 0°–20°S. These results are consistent with previous studies (Tsuda et al., 2000; Ratnam et al., 2004; Ern et al., 2008, 2011, 2018; Alexander and Tsuda, 2009; Hoffmann et al., 2013; John and Kumar, 2013).

This subsection can be summarized as follows:
(1) The GWPE appeared as strong peaks over the Tibetan Plateau in the boreal winter and over the Andes in the austral winter. The GWPE over the tropical regions was stronger throughout the

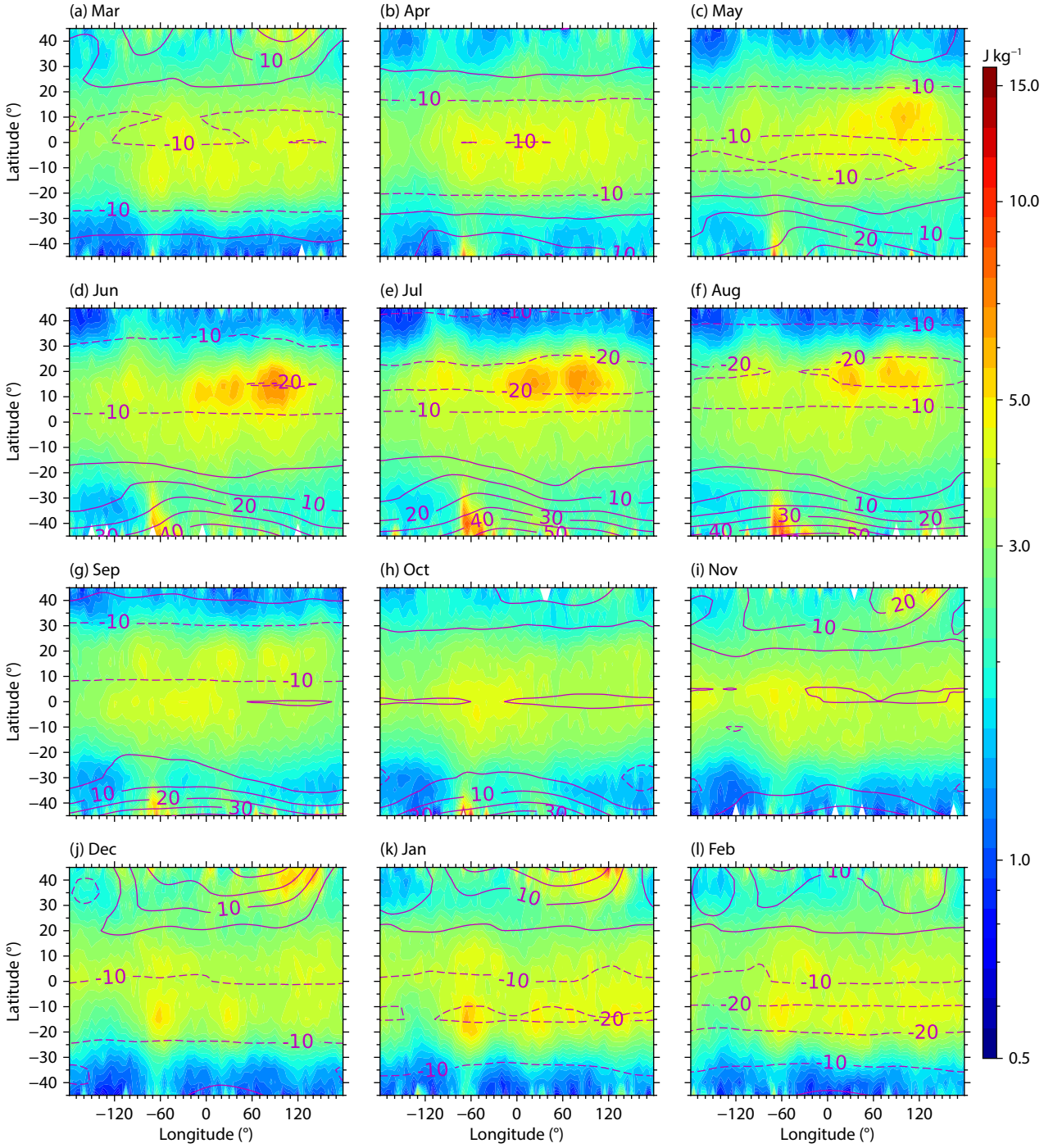

Figure 3. Maps of the monthly mean GWPE (color-filled contour) and zonal wind (contour lines, with a contour interval of 10 m/s) over 20–30 km in a composite year. The four rows (from top to bottom) are boreal spring, boreal summer, boreal autumn, and boreal winter, respectively. The thin solid and dashed lines and the thick solid contour lines represent the eastward and westward winds at 0 m/s, respectively.

composite year than at latitudes higher than 25°N and 25°S. These results are consistent with previous studies, which proves the credibility of our results on the fine structures of GWs.

(2) Unlike previous studies, the GWPE had a weak peak over the Rocky Mountains (~3–5 J/kg) from November to March.

3.2 GWPEs at ~40° N/S and Their Seasonal Dependencies

Figures 4–8 show the longitude–height distributions of the monthly mean GWPE in a composite year at ~40°S/N, ~20°S/N, and the Equator, respectively. To explore the physics, we overplotted the monthly mean zonal wind and average topographic elevation for each season and latitudinal band.

Figure 4 shows the longitude–height distributions of monthly mean GWPE in a composite year at ~40°S. This latitudinal band includes the Andes Mountains (~70°W), Africa (~30°E), and Australia (~120°E). The GWPE had prominent peaks (~10–15 J/kg) in the region of the Andes (40°–80°W) from April to October, with

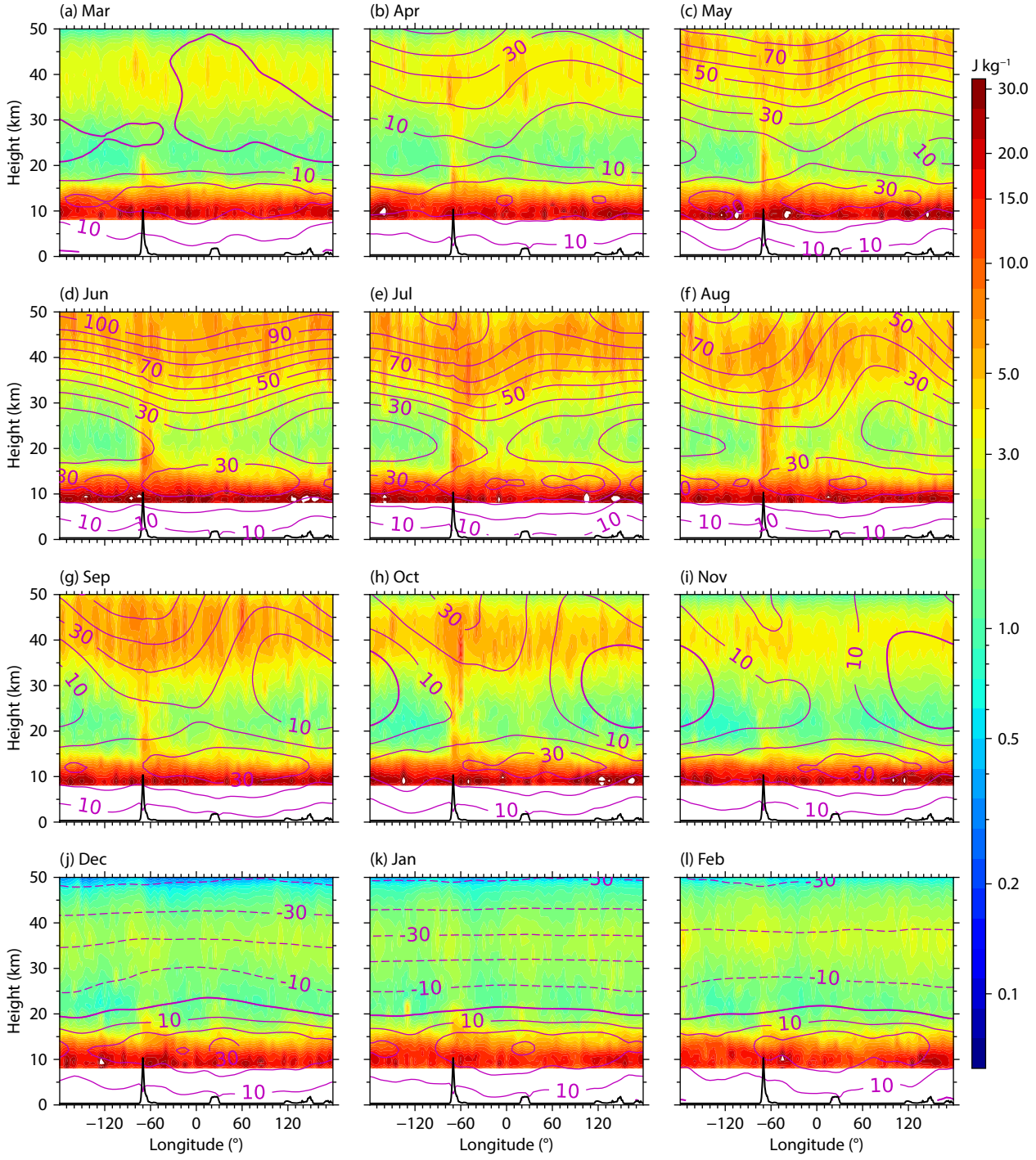

Figure 4. Longitude–height distributions of monthly mean GWPE (color-filled contours) at ~40°S in a composite year. In addition, in each panel, the monthly mean zonal wind calculated from MERRA-2 is plotted (the magenta contour lines in each panel with a contour interval of 20 m/s). The thin solid and dashed lines, and the thick solid contour lines represent the eastward and westward winds, 0 m/s, respectively. The average topographic elevations (multiplied by a factor of 5 for readability) at ~40°S are shown as black lines at the bottom of each panel.

a maximum of ~10–15 J/kg in the austral winter. This result also coincides with a prominent peak near the Andes from April to October, as shown in Figure 3. In March, the peaks extended to ~20 km, where the zonal wind speed was 0 m/s. From April to October, the peaks extended to 35 km, where the monthly mean zonal wind reached its minimum. In November, the peaks extended to 25 km. In general, the GWPE peaks at 15–20 km were more sporadic in longitude than were those at 20–35 km from March to August. The GWPE peaks in the austral winter were very sporadic throughout the entire altitude range of 15–35 km (extending eastward to 40°W). Compared with the GWPE at 15–35 km, the GWPE was stronger at 35–50 km throughout the longitudes and from May to September, when the zonal winds were stronger, with eastward speeds of higher than 30 m/s. Moreover, the lower boundaries of these peaks were consistent with fast zonal wind patterns, indicating that fast zonal winds (or strato-

spheric jets) play an important role in generating GWs and favor the westward-propagating GWs from a lower height. In contrast, the peaks were weak and reached lower heights (~30–45 km) during other months, when the zonal winds were weak or reversed from eastward to westward with increasing height. We observed no obvious relationship between the lower boundary of these weak peaks and the zonal winds.

Further examination showed strips embedded in the peak region of ~35–50 km. Some of these embedded strips (above the Andes, Africa, and Australia) might be related to topography, but they extended to a wider horizontal range. Other factors might be related to the strips located at ~10 km. These strips appear to be a consequence of the dense sampling of COSMIC-2, which had not been reported previously. Throughout the longitudes, the GWPE decreased from ~10 to ~15 km, reached a minimum in the middle stratosphere (~20–30 km), and then increased with the increasing height in all months and longitudes, indicating the dissipation of GWs at ~15–30 km.

Figure 5 shows the longitude–height distributions of monthly mean GWPE at ~40°N in a composite year. The Caucasus Mountains

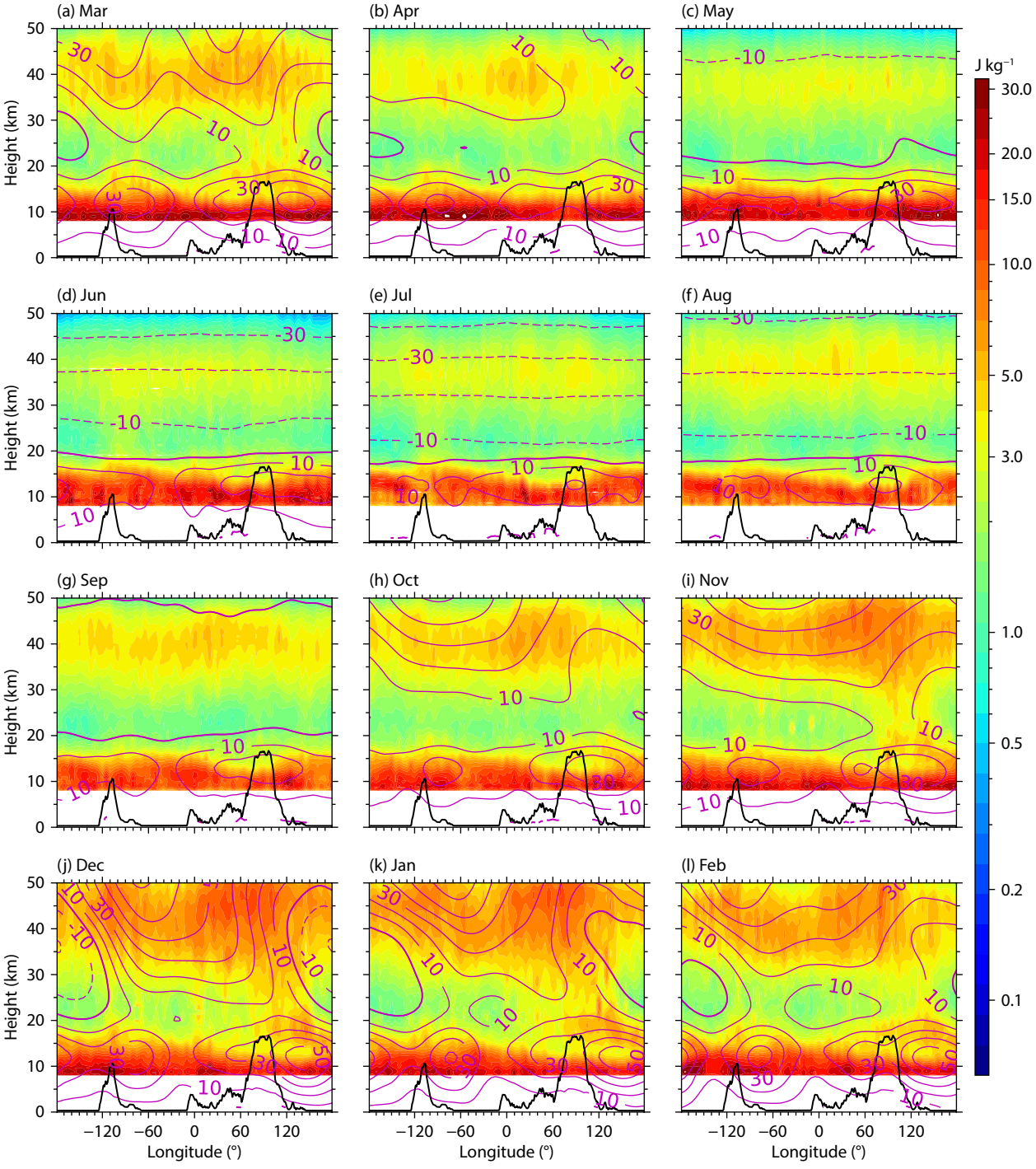

Figure 5. Same caption as in Figure 4 but at ~40°N.

(45°E), the Tianshan Mountains (70°E), the Tibetan Plateau (90°E), the Atlas Mountains (0°W/E), and the Rocky Mountains (110°W) are present in this latitudinal band. From November to March, the GWPE exhibited prominent peaks (~5–10 J/kg) near the Tibetan Plateau. These peaks shifted from the east of the Tibetan Plateau at ~20 km to its west at above 30 km. The westward shift of these peaks followed the eastward winds. Moreover, the decelerating eastward zonal wind and wind reversals appeared to prohibit the upward extension of the peaks to the east of the Tibetan Plateau. In contrast, the GWPE did not show a prominent peak from April to October. This result also coincides with the prominent peak near the Tibetan Plateau in Figure 3. Compared with the obvious peak of the GWPE over the Tibetan Plateau from November to March, the peaks of the GWPE above the Caucasus, Tianshan, Atlas, and Rocky Mountains are relatively weak (~3–8 J/kg). Notably, height variations of the peaks above the Rocky Mountains were similar to those above the Tibetan Plateau but had smaller magnitudes. The weak peak of the GWPE was just above the Rocky Mountains at ~15–20 km, but it extended to a wider horizontal range above 35 km.

A dissipation layer was observed in the middle stratosphere, which was similar to that at ~40°S. From November to March, the GWPE peaks followed the strong eastward zonal winds above the dissipation layer. The strips were also embedded in the GWPE peak regions above the dissipation layers. From April to October and above the dissipation layer, the GWPE peaks were weaker than those in other months. From June to August and at ~30–45 km, the longitudinal variations in the GWPE were positively correlated with topography, probably because MWs are prohibited by a zero wind speed at ~20 km. The dissipation of these GWs produces a body force that generates large-scale secondary GWs that spread around topographic regions.

This subsection can be summarized as follows:
(1) At ~40°N/S, we found that the dissipation layer was present in all seasons and in the middle stratosphere.
(2) In the upper stratosphere, the GWPE had stronger peaks throughout the longitudes from May to September at 40°S and from November to March at 40°N, which was related to the winter stratospheric jet.
(3) The figures show that the embedded strips in the upper stratosphere might be related to both topographic and nontopographic GW sources. We discuss the physics behind these phenomena in Section 4.

3.3 GWPEs at ~20°N/S and Their Seasonal Dependencies

Figure 6 shows the longitude–height distributions of the monthly mean GWPE at ~20°S in a composite year. This latitudinal band includes the northern Andes (70°W), Africa (20°E), and Australia (150°E). In the lower stratosphere and from May to October, the GWPE had a peak (~5–10 J/kg) above the northern Andes but had no peak above Africa and Australia. In the middle stratosphere, the GWPE was weaker than that in the lower and upper stratosphere throughout the longitudes during all months. However, weak peaks of the GWPE above the northern Andes, Africa, and Australia in the middle stratosphere were observed. These weak peaks extended into the upper stratosphere and spread over a wider longitudinal range. The height variations of the GWPE at ~20°S coincided with those at ~40°N/S. Specifically, the GWPE was weaker in the middle stratosphere than in the lower and upper stratosphere, indicating the presence of a dissipation layer in the middle stratosphere as a consequence of the decelerating of the eastward zonal wind and wind reversal. Unlike at ~40°S, no strips were embedded in the peaks in the upper stratosphere or at ~10 km, indicating that the longitudinal variations in GW sources were more uniform at ~20°S than at ~40°S, except for topographic sources.

Note that in the upper stratosphere and from May to November, the GWPE had a stronger peak in the longitudinal range between the northern Andes and Africa than to the east of the northern Andes and Australia. Moreover, the stronger peaks had shorter horizontal distances to Africa than to the northern Andes, probably because the GW of ~10 km could be ascribed to topographic and nontopographic sources. Both of these dissipated in the middle stratosphere as they propagated upward because of the zonal wind reversing from eastward to westward with increasing height. The dissipated GWs provide body forces that generate secondary GWs that propagate eastward and westward because of the weak zonal wind in the upper stratosphere. This, in turn, formed the GWPE peaks in the upper stratosphere and throughout the longitude. The stronger peak in the longitudinal range between the northern Andes and Africa might be a combined effect of the westward- and eastward-propagating secondary GWs generated from the body force above the northern Andes and Africa, respectively. Moreover, westward-propagating GWs may be dominant because the eastward zonal wind provides a favorable environment for them. Therefore, the stronger peak in the upper stratosphere had a shorter distance to Africa than to the northern Andes.

From December to February, the GWPE at ~35 km had peaks in the northern Andes, Africa, and Australia. These peaks were slightly stronger east of topographic peaks than west of them because the westward zonal wind provided favorable conditions for the eastward-propagating secondary GWs.

Figure 7 shows the longitude–height distributions of monthly mean GWPE at ~20°N in a composite year. In this latitudinal band, Mexico (~100°W), northern Africa (40°E), and southern Asia (100°E) had lower topographic elevations than did the other latitudinal bands. In the tropopause region (~10 km), the GWPE was stronger above the sea than above the topography during all months. Moreover, the longitudinal variations in the GWPE were more uniform from March to May and from December to February than in other months. Similar to that in other latitudes, a dissipation layer of GWs was also observed in the middle stratosphere. The GWPE then reached a peak in the upper stratosphere.

The longitudinal variations of the GWPE in the upper stratosphere depend on the month. In the boreal spring and winter, the longitudinal variations in the GWPE were more uniform, and the stronger peaks of the GWPE were above both the topography and sea. In the boreal summer, the three strongest peaks (~5–10 J/kg) of the GWPE coincidentally occurred above the topography (Mexico, northern Africa, and southern Asia) when the westward

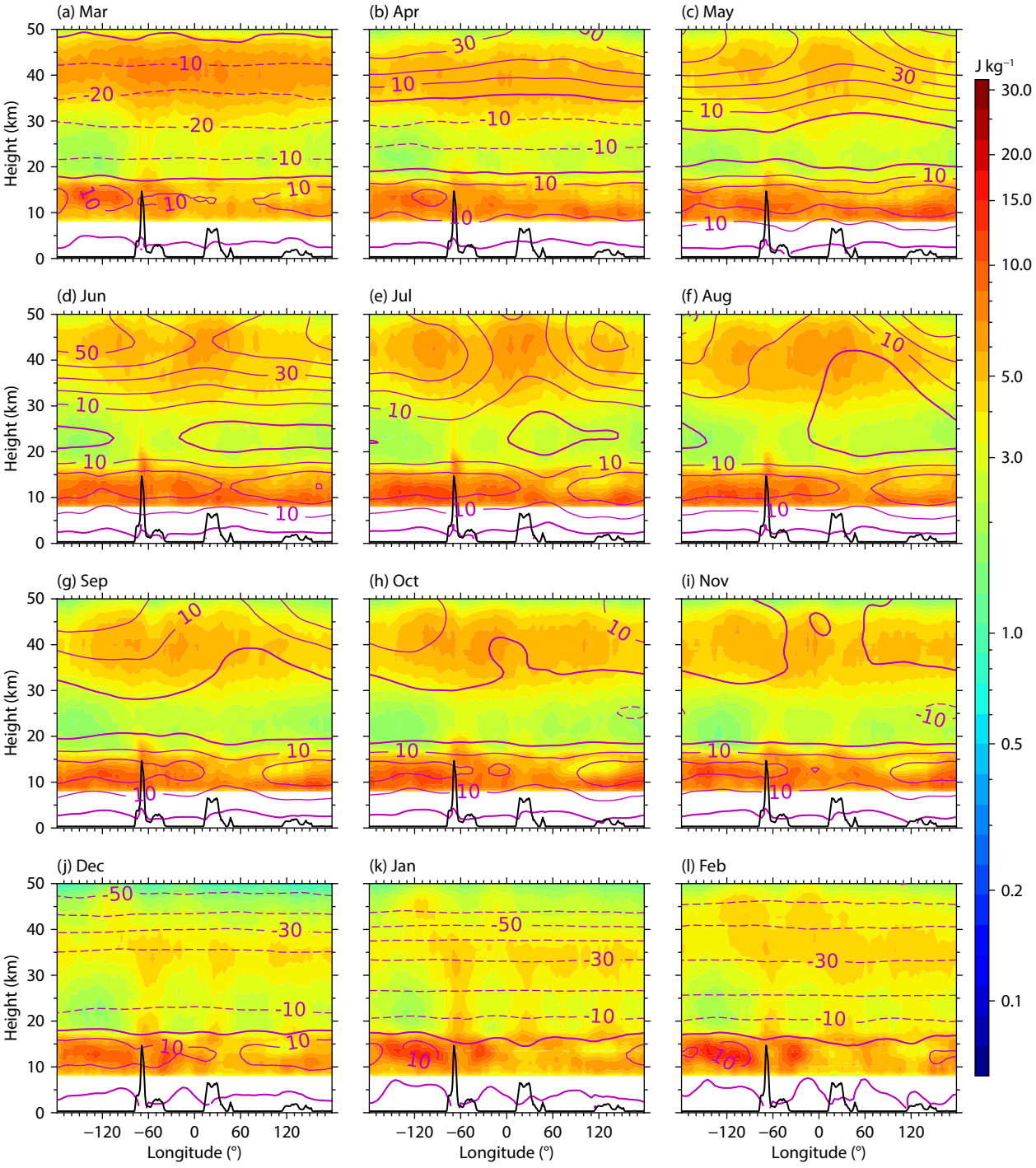

Figure 6. Same caption as in Figure 4 but at ~20°S.

zonal wind was stronger (>20 m/s). In the boreal autumn, the stronger GWPE peaks were mainly above the topography (northern Africa and southern Asia) and above the sea between the two topographies.

Therefore, the GWPE at ~20°N/S can be summarized as follows:

(1) The figures showed that the dissipation layer at ~20°N/S was also in the middle stratosphere and coincided with that at ~40°N/S.

(2) In the lower stratosphere, the GWPE had stronger peaks above the sea than above continents at ~20°N/S.

(3) In the upper stratosphere, the GWPE had three peaks, which were above the east of the topographies in the austral (at ~20°S) and boreal (at ~20°N) summers, when the zonal wind reversed from eastward in the lower stratosphere to westward in the upper stratosphere.

(4) In the upper stratosphere, the strongest GWPE peaks were above west Africa from May to November at ~20°S and above the west of southern Asia from September to March at ~20°N. The strongest peak might be a combined effect of nontopographic GWs and MWs, whereas the MW-induced secondary GWs played a dominant role.

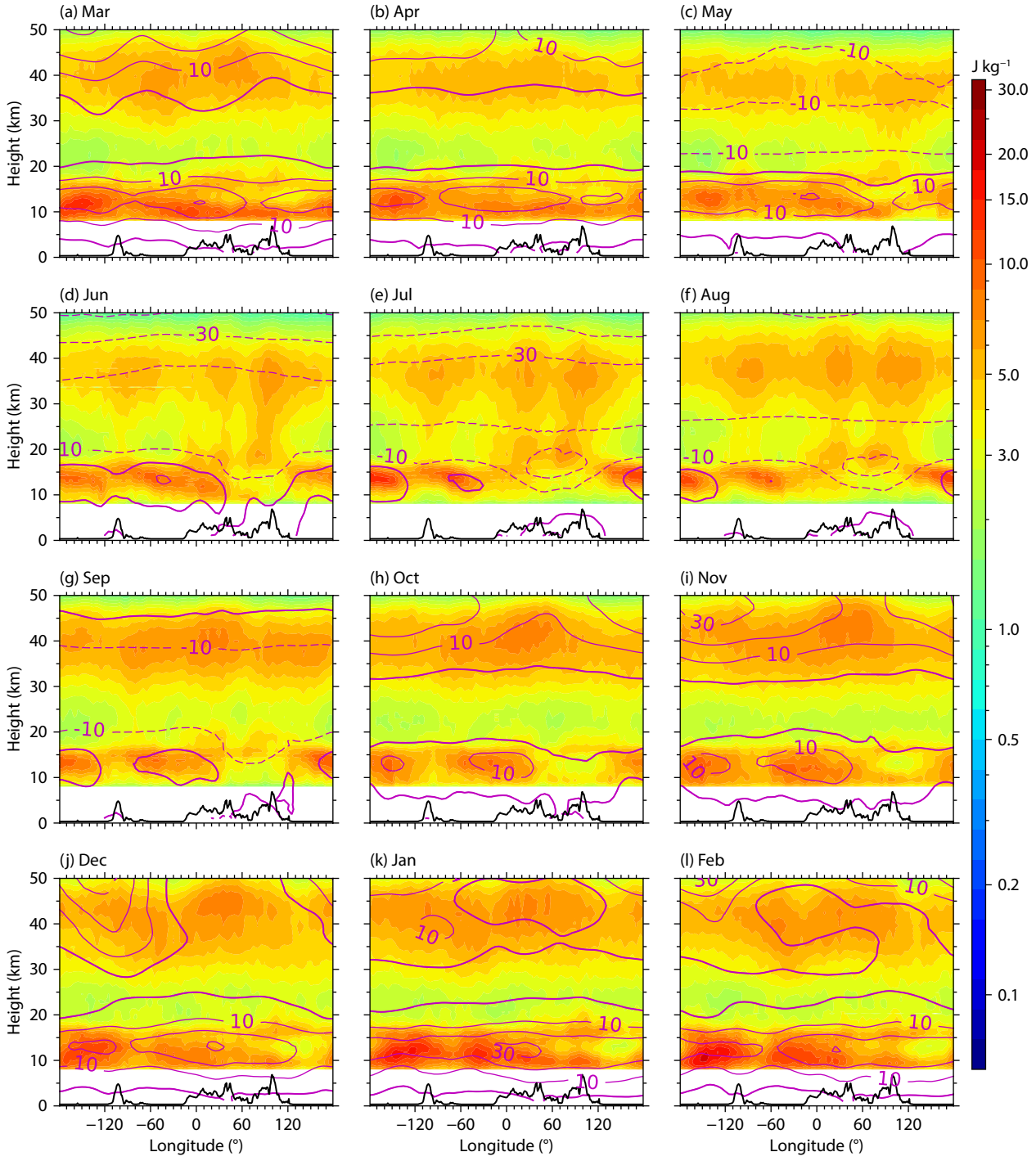

Figure 7. Same caption as in Figure 4 but at ~20°N.

3.4 GWPEs at the Equator and Their Seasonal Dependencies

Figure 8 shows the longitude–height distributions of the monthly mean GWPE at the Equator in a composite year. This latitudinal band includes the northern Andes (80°W), and Africa (40°E). In the lower stratosphere, the longitudinal distribution of the GWPE peaks was not related to the topography and sea. At 10–15 km, the GWPE in the Eastern Hemisphere was slightly weaker than in the Western Hemisphere because the zonal wind changes more frequently with height in the Eastern Hemisphere than in the Western Hemisphere. Compared with other latitudinal bands, the dissipation layer was weaker, and the height range of the dissipation layer varied significantly with longitude because of frequent changes in zonal wind with increasing height, which prohibited the upward-propagating GWs with both eastward and westward horizontal phase speeds. Only the GWs with high horizontal phase speeds could propagate upward. In the upper stratosphere, the GWPE peaks were mainly above the sea. The longitudinal variation of the GWPE was the strongest above the sea in the boreal summer because the horizontal phase speeds of GWs generated by convection had a wide spectral range. Although wind reversals filter out some of the GWs with slow horizontal phase speeds,

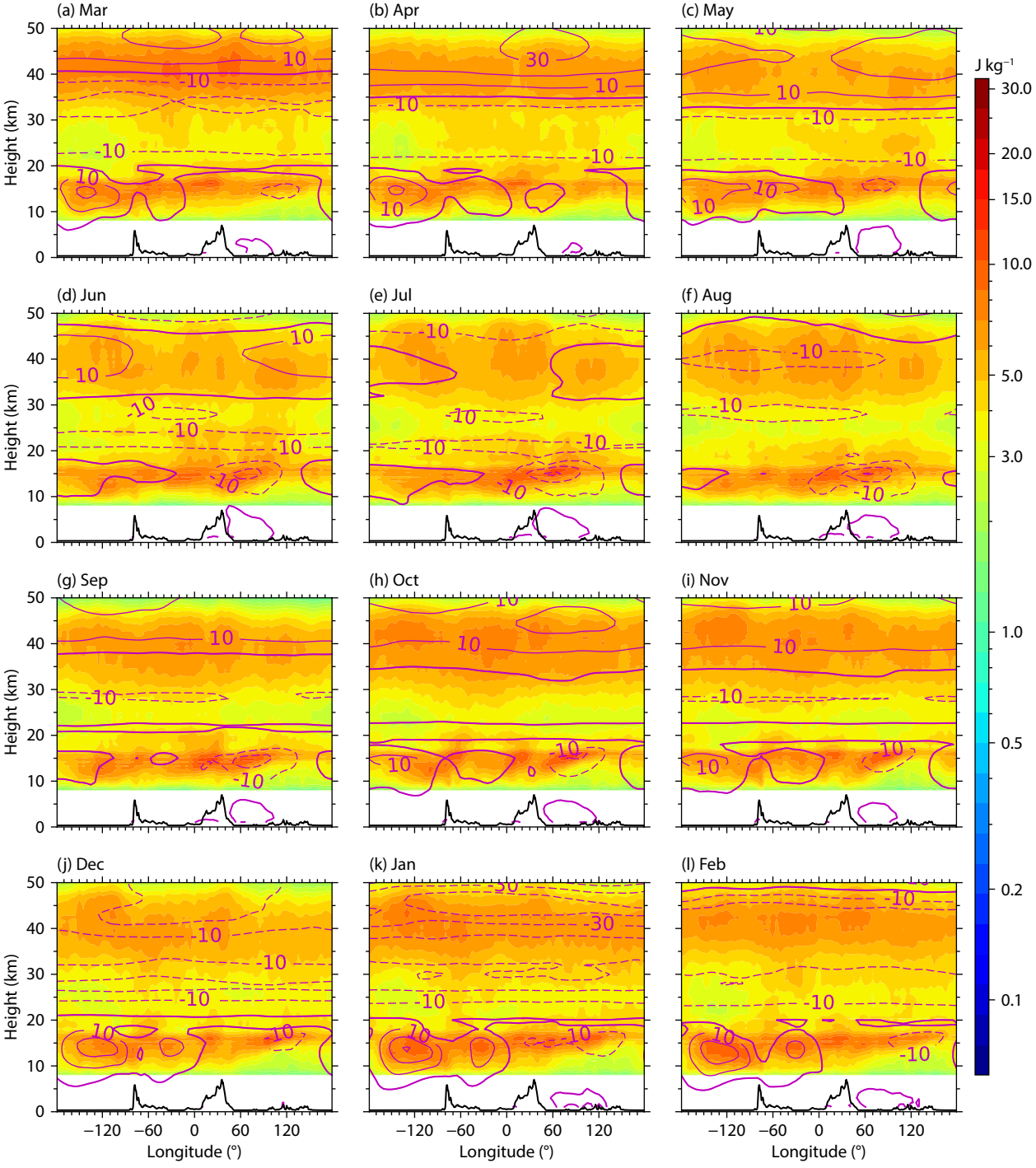

Figure 8. Same caption as in Figure 4 but at the Equator.

some of the GWs with high horizontal phase speeds propagated into the upper stratosphere. In the boreal autumn and winter, the GWPE in the Eastern Hemisphere was weaker than in the Western Hemisphere. This situation is similar to that in the lower stratosphere.

4. Discussion

The main features described in the previous section are the weak GWPE at 20–30 km and the strip structures embedded in the GWPE peak regions at ~40 km. Figure 9 shows the zonal mean GWPE, vertical wavelength, and zonal wind in a composite year in the five latitudinal bands. The weak GWPE at ~20–30 km, as shown in Figures 4–7, can also be observed in Figure 9. The weak GWPE at ~20–30 km has been observed in previous satellite observations. For example, Tsuda et al. (2000) showed a weak GWPE in the middle stratosphere when using GPS/MET temperature data from April 1995 to February 1997. Using the temperature profiles measured by the Solar Occultation for Ice Experiment (SOFIE) instrument onboard the Aeronomy of Ice in the Mesosphere (AIM) satellite from 2007 to 2013, Liu X et al. (2014) showed that the GWPE in all seasons of the polar region decreased in the lower stratosphere with increasing altitude and

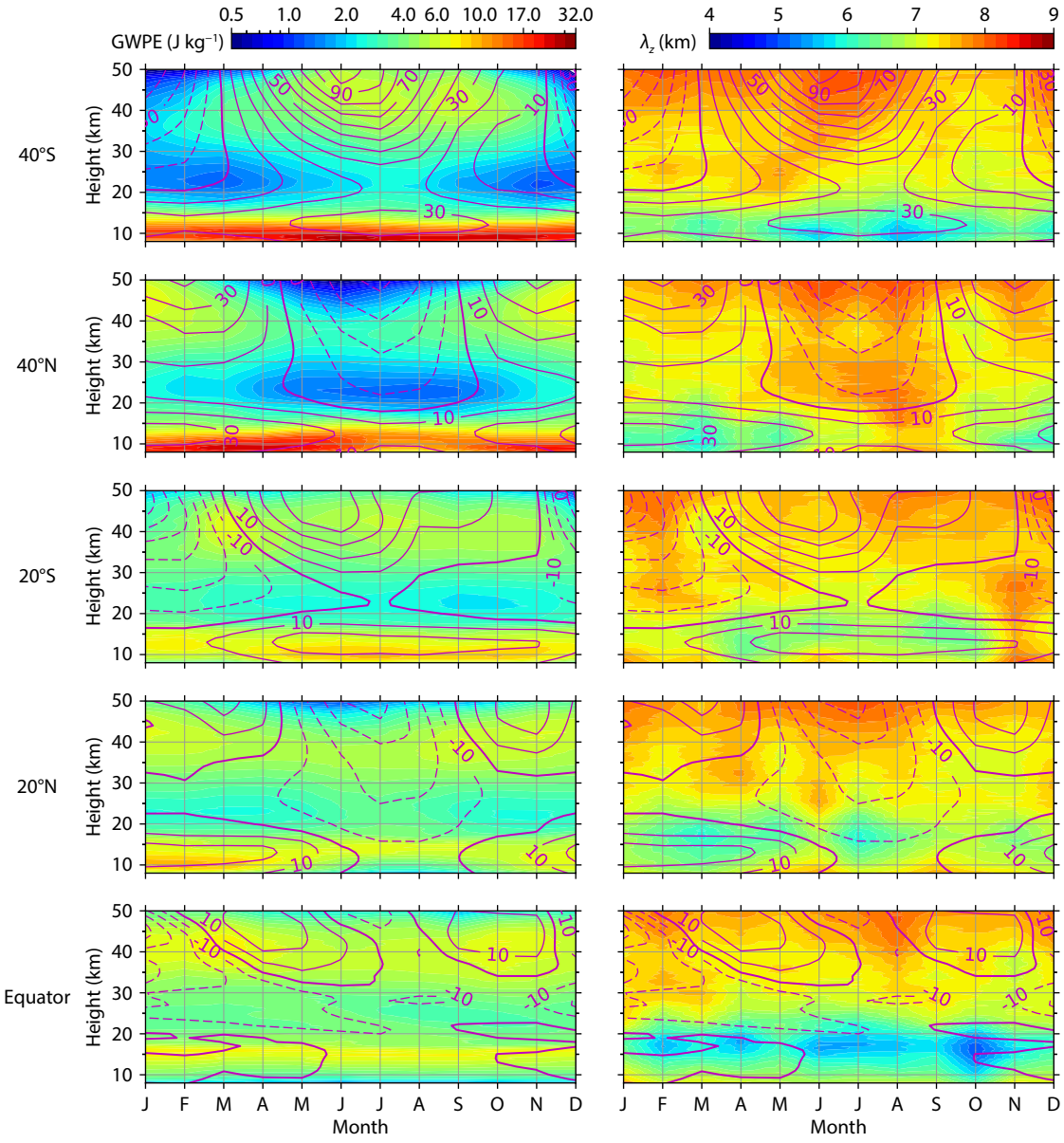

Figure 9. Cross-sections of GWPE (first column) and λ_z (second column) as a function of the monthly height at five latitudinal bands (at ~40°S/N, ~20°S/N, and the Equator). Also plotted in each panel is the monthly mean zonal wind calculated from MERRA-2 (the magenta contour lines in each panel with a contour interval of 20 m/s). The thin solid and dashed lines and the thick solid contour lines represent the eastward and westward winds, 0 m/s, respectively.

then increased in the upper stratosphere and mesosphere with increasing altitude, reaching its minimum at an altitude of ~25 km. The weak GWPE in the middle stratosphere may be due to the saturation of GWs or the loss of energy caused by nonlinear mutual damping with other waves, resulting in the transfer of the GWPE to the background flow or other waves (Liu X et al., 2008; Li T et al., 2010). Possible mechanisms can be ascribed to the saturation of GWs or the loss of energy caused by the nonlinear interactions with other waves, resulting in the transfer of the GWPE to the background flow or other waves (Liu X et al., 2008; Li T et al., 2010). According to these mechanisms and height-dependent wind structures, we propose that the decreasing zonal winds above the tropopause jet play an important role in dissipating GWs at ~20–30 km.

The GWs generated in the troposphere were hindered by the tropopause jet, where the eastward zonal wind speed was high (contour lines in Figure 9). The eastward jet acts as a critical layer for eastward-propagating GWs with a horizontal phase velocity slower than that of the jet. According to Equation (5.66) of Nappo (2002), the amplitude of the horizontal velocity perturbation ($\hat{u}$) becomes very high and the vertical wavelength becomes very small. The temperature perturbation is then very high because of $T' \approx (g/N)\,\hat{u}$ (Gubenko et al., 2008; Liu X et al., 2020). Thus, near the jet region, the vertical wavelengths of the GWs reached their minima and the GWPEs reached their maxima (Figure 9). It can be speculated that the remaining GWs above the jet region are composed of three components as follows:

(1) Westward-propagating GWs.

(2) Eastward-propagating GWs with a faster horizontal phase velocity (c_h). These GWs have smaller vertical wavenumbers ($|k_z|$) and longer vertical wavelengths (λ_z) according to $|k_z| = N/|c_h|$ (Equation (32) of Fritts and Alexander, 2003).
(3) Large-scale secondary-generated GWs, which have longer vertical wavelengths than primary GWs near the jet region (Vadas and Fritts, 2001).

The combination of these three components increases the vertical wavelength above the jet region (right column of Figure 9). Moreover, the remaining GWs above the jet region should have less energy than those near the jet region. This induces a weak GWPE above the jet region.

Strip structures embedded in the GWPE peak regions of ~40 km had not previously been reported. The COSMIC satellite provided approximately 2000 temperature profiles from 90°S to 90°N, and each bin had a size of 10° × 20° (latitude × longitude) of the average GWPE profiles in previous studies (Wang L and Geller, 2003; Alexander et al., 2008a; Alexander and Tsuda, 2009; Khaykin et al., 2015). However, the COSMIC-2 satellite provided approximately 6000 temperature profiles from 45°S to 45°N. From the dense samplings of the COSMIC-2 satellite, we used a bin size of 5° × 5° (latitude × longitude) for the average GWPE profiles, to show that besides the typical topographic regions of the Tibetan Plateau and Andes, the GWPE had peaks in the boreal winter above the Rocky Mountains. Finer longitudinal variations have not been observed in previous studies.

In addition, strip structures were observed above the sea during the austral winter (especially above 40°S). These strip structures, in addition to being related to topography, may also have originated from GWs generated by convection. The amplitude of the GWs generated by convection reaches its maximum near the troposphere. Affected by the tropopause jet (Liu HL, 2017), the GWs generated by convection become unstable and break, forming a dissipation layer at 20–30 km and generating secondary GWs that continue to propagate upward, resulting in an obvious longitudinal structure at ~40 km.

The occurrence of GWs in the stratosphere might also be related to local time for the aspects of both wave sources and background atmospheric environment. The local time-dependent wave sources are mainly related to the convection and flow over the topography. According to observations by the AIRS aboard NASA's Aqua satellite, Hoffmann et al. (2013) classified them into three types (convective, topography, and otherwise). Table 9 of Hoffmann et al. (2013) showed that the fractions of the topographic source were generally larger in the daytime than those at nighttime except in September and October. Especially from November to February, the fraction of the topographic source was 46.4% in the daytime, which is much larger than the 27.1% at nighttime. The fraction of convective source was generally larger at nighttime than those in the daytime except in September and October. Especially from November to February, the fraction of the convective source was 52.2% in the daytime, which is smaller than the 72.6% at nighttime.

The local time-dependent background atmospheric environment may be related to tides. This is because both the tidal wind and temperature can act as an environment in which GWs propagate. Previously, studies have shown that interactions between GWs and tides may favor or prohibit upward propagation of GWs depending on the phase match between the GWs and tides (Liu X et al., 2008). Senf and Achatz (2011) used a global ray-tracing model, highly simplified GW ensemble, and time-dependent background to obtain simulation results showing that the time-dependent background plays an important role in modulating the frequency and phase velocities of GWs. These simulation results revealed that the local time-dependent background can influence the characteristics of GWs and thus their distribution. To return to the COSMIC-2 observations, these observations provide almost a full 24 hours of local-time data within a day. These dense samplings in both local time and geography provide a good opportunity to study tides in the upper troposphere and lower stratosphere. Along with our present studies on GWs, the relationships between GWs and tides in this region can be studied well on a time scale of one day. This will be our future work.

5. Conclusions

Taking advantage of the dense sampling of the COSMIC-2 satellite, we derived the GWPE in the upper troposphere and stratosphere at 45°S–45°N from December 2019 to November 2022. We also studied the distribution of GWs as well as their longitudinal and seasonal dependencies. The mechanisms were explored by using the monthly mean zonal wind from MERRA-2 and topography data. The main findings are as follows.

First, the seasonal distributions of GWs over special topographies (the Andes, the Tibetan Plateau, and tropical regions) have patterns similar to those observed in previous studies, thereby verifying the correctness of our data processing method. In addition, we found weak peaks of GWPE above the Rocky Mountains and the fine structure of the longitudinal variations of GWPE even over the Tibetan Plateau and other mountains, such as the Atlas, Caucasus, and Tianshan Mountains.

Second, at ~40°N/S, the GWPE peaks occurred in the upper stratosphere above the topographic regions during the winter months of each hemisphere, and notably, the strips were embedded in the peaks at ~35–50 km. Some of these embedded strips (above the Andes, Africa, and Australia) were related to topography but extended to a wider horizontal range. Other factors may be related to the strips located at ~10 km. At ~20°N/S and in the upper stratosphere, the strongest GWPE peaks were observed above western Africa from May to November at ~20°S and above and west of southern Asia from September to March at ~20°N. The strongest peak might be a combined effect of nontopographic GWs and MWs, although secondary-generated MWs played a dominant role. At the Equator, the longitudinal variations of the GWPE had prominent peaks above the sea or in regions with the lowest sea level altitude, indicating that convection was the main source.

Third, our results indicated that dissipation layers, which were above the tropopause jet, provided the body force to generate secondary waves in the upper stratosphere, especially during the winter months of each hemisphere and at ~40°N/S and ~20°N/S.

The fine structures of the longitudinal variations and GWPE peaks above the Rocky, Atlas, Caucasus, and Tianshan Mountains provided new insights into the global distribution of GWs. Combining the dissipation layers observed in this study with those reported previously, the middle stratosphere may be another layer that should be emphasized when studying the vertical propagation of GWs from the lower atmosphere to the upper atmosphere or ionosphere because the vertically propagating GWs observed in the upper atmosphere might experience dissipation, break at several layers, or both, such as the middle stratosphere shown here and the upper mesosphere shown by Liu X et al. (2022) and Li QZ et al. (2022).

Acknowledgments

This work was supported by the National Natural Science Foundation of China (Grant Nos. 41831073, 42174196, and 42374205), the Project of Stable Support for Youth Team in Basic Research Field, Chinese Academy of Sciences (CAS; Grant No. YSBR-018), the Informatization Plan of CAS (Grant No. CAS-WX2021PY-0101), the Youth Cross Team Scientific Research project of the Chinese Academy of Sciences (Grant No. JCTD-2021-10) and the Open Research Project of Large Research Infrastructures of CAS titled "Study on the Interaction Between Low-/Mid-Latitude Atmosphere and Ionosphere Based on the Chinese Meridian Project." This work was also supported in part by the Specialized Research Fund and the Open Research Program of the State Key Laboratory of Space Weather.

Open Research

Data Availability Statement

The COSMIC-2 (Constellation Observing System for Meteorology, Ionosphere, and Climate-2) temperature data are available at https://cdaac-www.cosmic.ucar.edu/. The MERRA-2 (Modern-Era Retrospective Analysis for Research and Application, Version 2) wind data were accessed from https://goldsmr5.gesdisc.eosdis.nasa.gov/data/MERRA2/M2I3NVASM.5.12.4/.

References

Alexander, S. P., Tsuda, T., and Kawatani, Y. (2008a). COSMIC GPS observations of Northern Hemisphere winter stratospheric gravity waves and comparisons with an atmospheric general circulation model. *Geophys. Res. Lett.*, *35*(10), L10808. https://doi.org/10.1029/2008GL033174

Alexander, S. P., Tsuda, T., Kawatani, Y., and Takahashi, M. (2008b). Global distribution of atmospheric waves in the equatorial upper troposphere and lower stratosphere: COSMIC observations of wave mean flow interactions. *J. Geophys. Res.: Atmos.*, *113*(D24), D24115. https://doi.org/10.1029/2008JD010039

Alexander, S. P., and Tsuda, T. (2009). Recent advances in the study of stratospheric wave activity using COSMIC and CHAMP GPS-RO. In A. Steiner, et al. (Eds.), *New Horizons in Occultation Research: Studies in Atmosphere and Climate* (pp. 141–151). Berlin: Springer. https://doi.org/10.1007/978-3-642-00321-9_12

Alexander, S. P., Klekociuk, A. R., and Murphy, D. J. (2011). Rayleigh lidar observations of gravity wave activity in the winter upper stratosphere and lower mesosphere above Davis, Antarctica (69°S, 78°E). *J. Geophys. Res.: Atmos.*, *116*(D13), D13109. https://doi.org/10.1029/2010JD015164

Anthes, R., and Schreiner, W. (2019). Six new satellites watch the atmosphere over Earth's equator. *Eos, 100*. https://doi.org/10.1029/2019EO131779. Published on 30 August 2019.

Anthes, R. A., Bernhardt, P. A., Chen, Y., Cucurull, L., Dymond, K. F., Ector, D., Healy, S. B., Ho, S. P., Hunt, D. C., … Zeng, Z. (2008). The COSMIC/FORMOSAT-3 mission: Early results. *Bull. Am. Meteor. Soc.*, *89*(3), 313–334. https://doi.org/10.1175/BAMS-89-3-313

Bretherton, F. P. (1966). The propagation of groups of internal gravity waves in a shear flow. *Quart. J. Roy. Meteor. Soc.*, *92*(394), 466–480. https://doi.org/10.1002/qj.49709239403

Coy, L., Wargan, K., Molod, A. M., McCarty, W. R., and Pawson, S. (2016). Structure and dynamics of the Quasi-Biennial Oscillation in MERRA-2. *J. Climate*, *29*(14), 5339–5354. https://doi.org/10.1175/jcli-d-15-0809.1

Eckermann, S. D., Hirota, I., and Hocking, W. K. (1995). Gravity wave and equatorial wave morphology of the stratosphere derived from long-term rocket soundings. *Quart. J. Ror. Meteor. Soc.*, *121*(521), 149–186. https://doi.org/10.1002/qj.49712152108

Ern, M., Preusse, P., Alexander, M. J., and Warner, C. D. (2004). Absolute values of gravity wave momentum flux derived from satellite data. *J. Geophys. Res.: Atmos.*, *109*(D20), D20103. https://doi.org/10.1029/2004JD004752

Ern, M., Preusse, P., Krebsbach, M., Mlynczak, M. G., and Russell III, J. M. (2008). Equatorial wave analysis from SABER and ECMWF temperatures. *Atmos. Chem. Phys.*, *8*(4), 845–869. https://doi.org/10.5194/acp-8-845-2008

Ern, M., Preusse, P., Gille, J. C., Hepplewhite, C. L., Mlynczak, M. G., Russell III, J. M., and Riese, M. (2011). Implications for atmospheric dynamics derived from global observations of gravity wave momentum flux in stratosphere and mesosphere. *J. Geophys. Res.: Atmos.*, *116*(D19), D19107. https://doi.org/10.1029/2011JD015821

Ern, M., Hoffmann, L., and Preusse, P. (2017). Directional gravity wave momentum fluxes in the stratosphere derived from high-resolution AIRS temperature data. *Geophys. Res. Lett.*, *44*(1), 475–485. https://doi.org/10.1002/2016GL072007

Ern, M., Trinh, Q. T., Preusse, P., Gille, J. C., Mlynczak, M. G., Russell III, J. M. R., and Riese, M. (2018). GRACILE: A comprehensive climatology of atmospheric gravity wave parameters based on satellite limb soundings. *Earth Syst. Sci. Data*, *10*(2), 857–892. https://doi.org/10.5194/essd-10-857-2018

Faber, A., Llamedo, P., Schmidt, T., de la Torre, A., and Wickert, J. (2013). On the determination of gravity wave momentum flux from GPS radio occultation data. *Atmos. Meas. Tech.*, *6*(11), 3169–3180. https://doi.org/10.5194/amt-6-3169-2013

Fetzer, E. J., and Gille, J. C. (1994). Gravity wave variance in LIMS temperatures. Part I: Variability and comparison with background winds. *J. Atmos. Sci.*, *51*(17), 2461–2483. https://doi.org/10.1175/1520-0469(1994)051<2461:GWVILT>2.0.CO;2

Fjeldbo, G., Kliore, A. J., and Eshleman, V. R. (1971). The neutral atmosphere of Venus as studied with the Mariner V radio occultation experiments. *Astron. J.*, *76*(2), 123–140. https://doi.org/10.1086/111096

Fritts, D. C., and Nastrom, G. D. (1992). Sources of mesoscale variability of gravity waves. Part II: Frontal, convective, and jet stream excitation. *J. Atmos. Sci.*, *49*(2), 111–127. https://doi.org/10.1175/1520-0469(1992)049<0111:SOMVOG>2.0.CO;2

Fritts, D. C., Isler, J. R., and Andreassen, Ø. (1994). Gravity wave breaking in two and three dimensions: 2. Three-dimensional evolution and instability structure. *J. Geophys. Res.: Atmos.*, *99*(D4), 8109–8123. https://doi.org/10.1029/93JD03436

Fritts, D. C., and Alexander, M. J. (2003). Gravity wave dynamics and effects in the middle atmosphere. *Rev. Geophys.*, *41*(1), 1003. https://doi.org/10.1029/2001RG000106

Gelaro, R., McCarty, W., Suárez, M. J., Todling, R., Molod, A., Takacs, L., Randles, C. A., Darmenov, A., Bosilovich, M. G., … Zhao, B. (2017). The modern-era retrospective analysis for research and applications, Version 2 (MERRA-2). *J. Climate*, *30*(14), 5419–5454. https://doi.org/10.1175/JCLI-D-16-0758.1

Gubenko, V. N., Pavelyev, A. G., and Andreev, V. E. (2008). Determination of the intrinsic frequency and other wave parameters from a single vertical temperature or density profile measurement. *J. Geophys. Res.: Atmos.*, *113*(D8), D08109. https://doi.org/10.1029/2007JD008920

Heale, C. J., Bossert, K., Vadas, S. L., Hoffmann, L., Dörnbrack, A., Stober, G., Snively, J. B., and Jacobi, C. (2020). Secondary gravity waves generated by breaking mountain waves over Europe. *J. Geophys. Res.: Atmos.*, *125*(5),

e2019JD031662. https://doi.org/10.1029/2019JD031662

Hecht, J. H. (2004). Instability layers and airglow imaging. *Rev. Geophys.*, *42*(1), RG1001. https://doi.org/10.1029/2003RG000131

Hei, H., Tsuda, T., and Hirooka, T. (2008). Characteristics of atmospheric gravity wave activity in the polar regions revealed by GPS radio occultation data with CHAMP. *J. Geophys. Res.: Atmos.*, *113*(D4), D04107. https://doi.org/10.1029/2007JD008938

Hertzog, A., Souprayen, C., and Hauchecorne, A. (2001). Observation and backward trajectory of an inertio-gravity wave in the lower stratosphere. *Ann. Geophys.*, *19*(9), 1141–1155. https://doi.org/10.5194/angeo-19-1141-2001

Hindley, N. P., Wright, C. J., Smith, N. D., and Mitchell, N. J. (2015). The southern stratospheric gravity wave hot spot: Individual waves and their momentum fluxes measured by COSMIC GPS-RO. *Atmos. Chem. Phys.*, *15*(14), 7797–7818. https://doi.org/10.5194/acp-15-7797-2015

Hines, C. O. (1960). Internal atmospheric gravity waves at ionospheric heights. *Can. J. Phys.*, *38*(11), 1441–1481. https://doi.org/10.1139/p60-150

Ho, S. P., Zhou, X. J., Shao, X., Zhang, B., Adhikari, L., Kireev, S., He, Y. X., Yoe, J. G., Xia-Serafino, W., and Lynch, E. (2020). Initial assessment of the COSMIC-2/FORMOSAT-7 neutral atmosphere data quality in NESDIS/STAR using in situ and satellite data. *Remote Sens.*, *12*(24), 4099. https://doi.org/10.3390/rs12244099

Hoffmann, L., Xue, X., and Alexander, M. J. (2013). A global view of stratospheric gravity wave hotspots located with Atmospheric Infrared Sounder observations. *J. Geophys. Res.: Atmos.*, *118*(2), 416–434. https://doi.org/10.1029/2012JD018658

Holton, J. R. (1983). The influence of gravity wave breaking on the general circulation of the middle atmosphere. *J. Atmos. Sci.*, *40*(10), 2497–2507. https://doi.org/10.1175/1520-0469(1983)040<2497:TIOGWB>2.0.CO;2

Horinouchi, T., and Tsuda, T. (2009). Spatial structures and statistics of atmospheric gravity waves derived using a heuristic vertical cross-section extraction from COSMIC GPS radio occultation data. *J. Geophys. Res.: Atmos.*, *114*(D16), D16110. https://doi.org/10.1029/2008JD011068

Isler, J. R., Fritts, D. C., Andreassen, Ø., and Wasberg, C. E. (1994). Gravity wave breaking in two and three dimensions: 3. Vortex breakdown and transition to isotropy. *J. Geophys. Res.: Atmos.*, *99*(D4), 8125–8137. https://doi.org/10.1029/93JD03437

John, S. R., and Kumar, K. K. (2013). A discussion on the methods of extracting gravity wave perturbations from space-based measurements. *Geophys. Res. Lett.*, *40*(10), 2406–2410. https://doi.org/10.1002/grl.50451

Khaykin, S. M., Hauchecorne, A., Mzé, N., and Keckhut, P. (2015). Seasonal variation of gravity wave activity at midlatitudes from 7 years of COSMIC GPS and Rayleigh lidar temperature observations. *Geophys. Res. Lett.*, *42*(4), 1251–1258. https://doi.org/10.1002/2014GL062891

Kogure, M., Yue, J., Nakamura, T., Hoffmann, L., Vadas, S. L., Tomikawa, Y., Ejiri, M. K., and Janches, D. (2020). First direct observational evidence for secondary gravity waves generated by mountain waves over the Andes. *Geophys. Res. Lett.*, *47*(17), e2020GL088845. https://doi.org/10.1029/2020GL088845

Kursinski, E. R., Hajj, G. A., Schofield, J. T., Linfield, R. P., and Hardy, K. R. (1997). Observing Earth's atmosphere with radio occultation measurements using the Global Positioning System. *J. Geophys. Res.: Atmos.*, *102*(D19), 23429–23465. https://doi.org/10.1029/97jd01569

Li, Q. Z., Xu, J. Y., Liu, H. L., Liu, X., and Yuan, W. (2022). How do gravity waves triggered by a typhoon propagate from the troposphere to the upper atmosphere?. *Atmos. Chem. Phys.*, *22*(18), 12077–12091. https://doi.org/10.5194/acp-22-12077-2022

Li, T., Leblanc, T., McDermid, I. S., Wu, D. L., Dou, X. K., and Wang, S. (2010). Seasonal and interannual variability of gravity wave activity revealed by long-term lidar observations over Mauna Loa Observatory, Hawaii. *J. Geophys. Res.: Atmos.*, *115*(D13), D13103. https://doi.org/10.1029/2009JD013586

Liu, H. L. (2017). Large wind shears and their implications for diffusion in regions with enhanced static stability: The mesopause and the tropopause. *J. Geophys. Res.: Atmos.*, *122*(18), 9579–9590. https://doi.org/10.1002/2017JD026748

Liu, X., Xu, J. Y., Liu, H. L., and Ma, R. P. (2008). Nonlinear interactions between gravity waves with different wavelengths and diurnal tide. *J. Geophys. Res.: Atmos.*, *113*(D8), D08112. https://doi.org/10.1029/2007JD009136

Liu, X., Yue, J., Xu, J. Y., Wang, L., Yuan, W., Russell III, J. M., and Hervig, M. E. (2014). Gravity wave variations in the polar stratosphere and mesosphere from SOFIE/AIM temperature observations. *J. Geophys. Res.: Atmos.*, *119*(12), 7368–7381. https://doi.org/10.1002/2013JD021439

Liu, X., Yue, J., Xu, J. Y., Garcia, R. R., Russell III, J. M., Mlynczak, M., Wu, D. L., and Nakamura, T. (2017). Variations of global gravity waves derived from 14 years of SABER temperature observations. *J. Geophys. Res.: Atmos.*, *122*(12), 6231–6249. https://doi.org/10.1002/2017JD026604

Liu, X., Xu, J. Y., Yue, J., Vadas, S. L., and Becker, E. (2019). Orographic primary and secondary gravity waves in the middle atmosphere from 16-year SABER observations. *Geophys. Res. Lett.*, *46*(8), 4512–4522. https://doi.org/10.1029/2019GL082256

Liu, X., Xu, J. Y., Yue, J., and Liu, H. L. (2020). Gravity-wave-perturbed wind shears derived from SABER temperature observations. *Atmos. Chem. Phys.*, *20*(22), 14437–14456. https://doi.org/10.5194/acp-20-14437-2020

Liu, X., Xu, J. Y., Yue, J., and Kogure, M. (2022). Persistent layers of enhanced gravity wave dissipation in the upper mesosphere revealed from SABER observations. *Geophys. Res. Lett.*, *49*(5), e2021GL097038. https://doi.org/10.1029/2021GL097038

Lomb, N. R. (1976). Least-squares frequency analysis of unequally spaced data. *Astrophys. Space Sci.*, *39*(2), 447–462. https://doi.org/10.1007/BF00648343

Manney, G. L., and Hegglin, M. I. (2018). Seasonal and regional variations of long-term changes in upper-tropospheric jets from reanalyses. *J. Climate*, *31*(1), 423–448. https://doi.org/10.1175/jcli-d-17-0303.1

Marks, C. J., and Eckermann, S. D. (1995). A three-dimensional nonhydrostatic ray-tracing model for gravity waves: Formulation and preliminary results for the middle atmosphere. *J. Atmos. Sci.*, *52*(11), 1959–1984. https://doi.org/10.1175/1520-0469(1995)052<1959:atdnrt>2.0.co;2

Nappo, C. J. (2002). *An Introduction to Atmospheric Gravity Waves* (pp. 47–84). San Diego: Academic Press.

Preusse, P., Eckermann, S. D., and Offermann, D. (2000). Comparison of global distributions of zonal-mean gravity wave variance inferred from different satellite instruments. *Geophys. Res. Lett.*, *27*(23), 3877–3880. https://doi.org/10.1029/2000gl011916

Preusse, P., Eckermann, S. D., and Ern, M. (2008). Transparency of the atmosphere to short horizontal wavelength gravity waves. *J. Geophys. Res.: Atmos.*, *113*(D24), D24104. https://doi.org/10.1029/2007JD009682

Preusse, P., Eckermann, S. D., Ern, M., Oberheide, J., Picard, R. H., Roble, R. G., Riese, M., Russell III, J. M., and Mlynczak, M. G. (2009). Global ray tracing simulations of the SABER gravity wave climatology. *J. Geophys. Res.: Atmos.*, *114*(D8), D08126. https://doi.org/10.1029/2008JD011214

Randel, W. J., Wu, F., and Podglajen, A. (2021). Equatorial waves, diurnal tides and small-scale thermal variability in the tropical lower stratosphere from COSMIC-2 radio occultation. *J. Geophys. Res.: Atmos.*, *126*(7), e2020JD033969. https://doi.org/10.1029/2020JD033969

Ratnam, M. V., Tetzlaff, G., and Jacobi, C. (2004). Global and seasonal variations of stratospheric gravity wave activity deduced from the *CHAMP*/GPS satellite. *J. Atmos. Sci.*, *61*(13), 1610–1620. https://doi.org/10.1175/1520-0469(2004)061<1610:gasvos>2.0.co;2

Rocken, C., Anthes, R., Exner, M., Hunt, D., Sokolovskiy, S., Ware, R., Gorbunov, M., Schreiner, W., Feng, D., … Zou, X. (1997). Analysis and validation of GPS/MET data in the neutral atmosphere. *J. Geophys. Res.: Atmos.*, *102*(D25), 29849–29866. https://doi.org/10.1029/97JD02400

Sato, K. (1993). Small-scale wind disturbances observed by the MU radar during the passage of Typhoon Kelly. *J. Atmos. Sci.*, *50*(4), 518–537. https://doi.org/10.1175/1520-0469(1993)050<0518:SSWDOB>2.0.CO;2

Scherllin-Pirscher, B., Steiner, A. K., Kirchengast, G., Kuo, Y. H., and Foelsche, U. (2011). Empirical analysis and modeling of errors of atmospheric profiles from GPS radio occultation. *Atmos. Meas. Tech.*, *4*(9), 1875–1890. https://doi.org/10.5194/amt-4-1875-2011

Schoon, L., and Zülicke, C. (2018). A novel method for the extraction of local

gravity wave parameters from gridded three-dimensional data: Description, validation, and application. *Atmos. Chem. Phys.*, *18*(9), 6971–6983. https://doi.org/10.5194/acp-18-6971-2018

Schreiner, W. S., Weiss, J. P., Anthes, R. A., Braun, J., Chu, V., Fong, J., Hunt, D., Kuo, Y. H., Meehan, T., … Zeng, Z. (2020). COSMIC-2 radio occultation constellation: First results. *Geophys. Res. Lett.*, *47*(4), e2019GL086841. https://doi.org/10.1029/2019GL086841

Senf, F., and Achatz, U. (2011). On the impact of middle-atmosphere thermal tides on the propagation and dissipation of gravity waves. *J. Geophys. Res.: Atmos.*, *116*(D24), D24110. https://doi.org/10.1029/2011JD015794

Shepherd, T. G. (2002). Issues in stratosphere–troposphere coupling. *J. Meteor. Soc. Japan*, *80*(4B), 769–792. https://doi.org/10.2151/jmsj.80.769

Torrence, C., and Compo, G. P. (1998). A practical guide to wavelet analysis. *Bull. Am. Meteor. Soc.*, *79*(1), 61–78. https://doi.org/10.1175/1520-0477(1998)079<0061:APGTWA>2.0.CO;2

Trinh, Q. T., Ern, M., Doornbos, E., Preusse, P., and Riese, M. (2018). Satellite observations of middle atmosphere–thermosphere vertical coupling by gravity waves. *Ann. Geophys.*, *36*(2), 425–444. https://doi.org/10.5194/angeo-36-425-2018

Tsuda, T., Murayama, Y., Yamamoto, M., Kato, S., and Fukao, S. (1990). Seasonal variation of momentum flux in the mesosphere observed with the MU radar. *Geophys. Res. Lett.*, *17*(6), 725–728. https://doi.org/10.1029/GL017i006p00725

Tsuda, T., Nishida, M., Rocken, C., and Ware, R. H. (2000). A global morphology of gravity wave activity in the stratosphere revealed by the GPS occultation data (GPS/MET). *J. Geophys. Res.: Atmos.*, *105*(D6), 7257–7273. https://doi.org/10.1029/1999jd901005

Vadas, S. L., and Fritts, D. C. (2001). Gravity wave radiation and mean responses to local body forces in the atmosphere. *J. Atmos. Sci.*, *58*(16), 2249–2279. https://doi.org/10.1175/1520-0469(2001)058<2249:GWRAMR>2.0.CO;2

Vadas, S. L., and Fritts, D. C. (2002). The importance of spatial variability in the generation of secondary gravity waves from local body forces. *Geophys. Res. Lett.*, *29*(20), 1984. https://doi.org/10.1029/2002GL015574

Vadas, S. L., Zhao, J., Chu, X. Z., and Becker, E. (2018). The excitation of secondary gravity waves from local body forces: Theory and observation. *J. Geophys. Res.: Atmos.*, *123*(17), 9296–9325. https://doi.org/10.1029/2017JD027970

Wang, L., and Geller, M. A. (2003). Morphology of gravity-wave energy as observed from 4 years (1998–2001) of high vertical resolution U.S. radiosonde data. *J. Geophys. Res.: Atmos.*, *108*(D16), 4489. https://doi.org/10.1029/2002JD002786

Wickert, J., Reigber, C., Beyerle, G., König, R., Marquardt, C., Schmidt, T., Grunwaldt, L., Galas, R., Meehan, T. K., … Hocke, K. (2001). Atmosphere sounding by GPS radio occultation: First results from CHAMP. *Geophys. Res. Lett.*, *28*(17), 3263–3266. https://doi.org/10.1029/2001GL013117

Wickert, J., Beyerle, G., König, R., Heise, S., Grunwaldt, L., Michalak, G., Reigber, C., and Schmidt, T. (2005). GPS radio occultation with CHAMP and GRACE: A first look at a new and promising satellite configuration for global atmospheric sounding. *Ann. Geophys.*, *23*(3), 653–658. https://doi.org/10.5194/angeo-23-653-2005

Yan, X. P., Arnold, N., and Remedios, J. (2010). Global observations of gravity waves from High Resolution Dynamics Limb Sounder temperature measurements: A yearlong record of temperature amplitude and vertical wavelength. *J. Geophys. Res.: Atmos.*, *115*(D10), D10113. https://doi.org/10.1029/2008JD011511

Zeng, X. Y., Xue, X. H., Dou, X. K., Liang, C., and Jia, M. J. (2017). COSMIC GPS observations of topographic gravity waves in the stratosphere around the Tibetan Plateau. *Sci. China Earth Sci.*, *60*(1), 188–197. https://doi.org/10.1007/s11430-016-0065-6